Materials Today Bio 26 (2024) 101019

Contents lists available at ScienceDirect

Materials Today Bio

journal homepage: www.journals.elsevier.com/materials-today-bio

MRI-guided cell membrane-camouflaged bimetallic coordination nanoplatform for combined tumor phototherapy

Mengyang Zhou [1], Yifei Wang [1], Yaning Xia, Yinhua Li, Jianfeng Bao, Yong Zhang, Jingliang Cheng, Yupeng Shi [*]

Department of MRI, The First Affiliated Hospital of Zhengzhou University, Henan Key Laboratory of Functional Magnetic Resonance Imaging and Molecular Imaging, Zhengzhou, 450052, China

ARTICLE INFO

Keywords:
Metal chelation
MR imaging
Photodynamic therapy
Photothermal therapy
Homologous targeting

ABSTRACT

Nanotechnology for tumor diagnosis and optical therapy has attracted widespread interest due to its low toxicity and convenience but is severely limited due to uncontrollable tumor targeting. In this work, homologous cancer cell membrane-camouflaged multifunctional hybrid metal coordination nanoparticles (DRu/Gd@CM) were prepared for MRI-guided photodynamic therapy (PDT) and photothermal therapy (PTT) of tumors. Bimetallic coordination nanoparticles are composed of three functional modules: dopamine, Ru(dcbpy)$_3$Cl$_2$ and GdCl$_3$, which are connected through 1,4-Bis[(1H-imidazole-1-yl)methyl]benzene (BIX). Their morphology can be easily controlled by adjusting the ratio of precursors. Optimistically, the intrinsic properties of the precursors, including the photothermal properties of polydopamine (PDA), the magnetic resonance (MR) response of Gd^{3+}, and the singlet oxygen generation of Ru(dcbpy)$_3$Cl$_2$, are well preserved in the hybrid metal nanoparticles. Furthermore, the targeting of homologous cancer cell membranes enables these coordinated nanoparticles to precisely target tumor cells. The MR imaging capabilities and the combination of PDT and PTT were demonstrated in *in vitro* experiments. In addition, *in vivo* experiments indicated that the nanoplatform showed excellent tumor accumulation and therapeutic effects on mice with subcutaneous tumors, and could effectively eliminate tumors within 14 days. Therefore, it expanded the new horizon for the preparation of modular nanoplatform and imaging-guided optical therapy of tumors.

1. Introduction

Optical therapy, recognized for its light-controlled, non-invasive, and low-toxicity properties, has garnered considerable interest and undergone significant advancements [1]. PDT and PTT are the two main optical treatments for tumors [2,3]. In particular, PDT uses radiation, oxygen, and photosensitizers to produce cytotoxic reactive oxygen species (ROS) like hydroxyl radicals (•OH), superoxide radicals (•O$_2^-$), and singlet oxygen (^{1}O$_2$), which effectively destroying tumor cells [4,5]. Photosensitizers are pivotal in this process, which directly affects the effectiveness of treatment. Organic variants, such as porphyrins and cyanine dyes, are prevalent in PDT due to their biocompatibility and efficiency in singlet oxygen production. Yet, their drawbacks, including limited water solubility and photobleaching susceptibility, hinder their broader application [6,7]. Transition metal complexes, notably ruthenium-polypyridine complexes, outshine their organic counterparts by offering superior thermal and photostability, water solubility, and ROS production capabilities, marking them as promising next-gen photosensitizers [8,9]. On the other hand, PTT leverages photothermal agents to transform light into heat, exploiting the heat vulnerability of tumor cells for elimination. The effectiveness of PTT hinges on the photothermal agent's conversion efficiency [10,11]. Several potent photothermal agents, both inorganic (e.g., graphene, noble metals, alloy nanoparticles) and organic (e.g., polypyrrole, porphyrin, polydopamine/PDA), have been established, and their clinical efficacy in tumor ablation is well-documented [12–16].

Though there's been extensive research on PDT and PTT for tumor treatment, the singular function and suboptimal efficacy of each method when used in isolation hamper the evolution of phototherapy. The integration of PDT and PTT aims to offset PTT's heat shock effect and PDT's tumor hypoxia, achieving a synergistic outcome that elevates tumor phototherapy's effectiveness [17–19]. Moreover, challenges in

---

[*] Corresponding author.
E-mail address: shiyup@zzu.edu.cn (Y. Shi).

[1] These authors have contributed equally to this work and share first authorship.

https://doi.org/10.1016/j.mtbio.2024.101019
Received 14 December 2023; Received in revised form 18 February 2024; Accepted 5 March 2024

visualizing tumor tissues and tracking photosensitizer distribution and metabolism curtail phototherapy's progress [20–22]. By integrating photosensitizers or photothermal agents with polymers or embedding them in nanocarriers, enhanced tumor targeting is achieved via the enhanced permeability and retention (EPR) effect, while simultaneously allowing visual imaging. Concurrently, precise imaging techniques enable accurate laser application, minimizing damage to healthy tissues and amplifying phototherapy's safety [23–25]. Hence, pioneering imaging-guided tumor phototherapies is imperative.

A pivotal aspect of image-guided therapy is crafting matrices that offer multifunctional capabilities. Metal-doped nanomaterials, in recent developments, have been synthesized with both imaging and therapeutic features. Coordination nanoparticles, hybrids of metal ions and multidentate ligands, stand out due to their remarkable functional integration, adjustable composition, size, and form. Such characteristics have made them instrumental in gas adsorption and storage, separation, and catalysis [26–30]. Their versatility further extends to various biological applications, encompassing early cancer detection, phototherapy, drug delivery, and imaging-guided therapy, especially when response-triggering functions are incorporated [31–33]. Yet, the synthesis of multifunctional coordination nanoparticles, via seamless integration of functional units, remains intricate. Furthermore, the immune system often identifies and purges nanoparticles due to their heterogeneity [34,35]. Thus, ensuring nanoparticles remain inconspicuous within the immune system is crucial. Several nanoparticles have been enhanced with group-targeting entities like antibodies and peptides to optimize nanodrugs [36–38]. Despite this, such modified nanoparticles often exhibit limited specificity, binding affinity, and short blood residence times at tumor sites. Hence, there's a pressing need to refine the concealment, targeting precision, and circulation longevity of these nanoparticles. A burgeoning strategy involves leveraging cell membrane camouflage technology for designing nanodrug systems tailored for disease diagnosis and treatment. Vesicles derived from various cell membranes, such as cancer cells, red blood cells, platelets, and stem cells, have been under rigorous investigation [39–41]. These biomimetic nanoparticles can enhance drug stability, elude immune detection, and extend blood circulation. Notably, the adhesion molecules present on cancer cell membranes, like adhesion proteins and integrins, grant them innate recognition and targeting capabilities [42]. Thus, leveraging homologous targeting holds promise for impactful tumor interventions.

In this study, we delineate the fabrication of Ru, Gd combined metal coordination nanoparticles via one-step metal chelation processing of a dopamine, Gd^{3+}, and $Ru(dcbpy)_3Cl_2$ blend in the company of the BIX ligand. This was followed by a homogenous cell membrane application through a physical extrusion method, resulting in a nanoplatform (DRu/Gd@CM NPs) purposed for imaging-guided optical therapy (as illustrated in Scheme 1). The coordinated nanoparticles' dimensions and structure are dictated by the precursor module ratios. Intriguingly, the

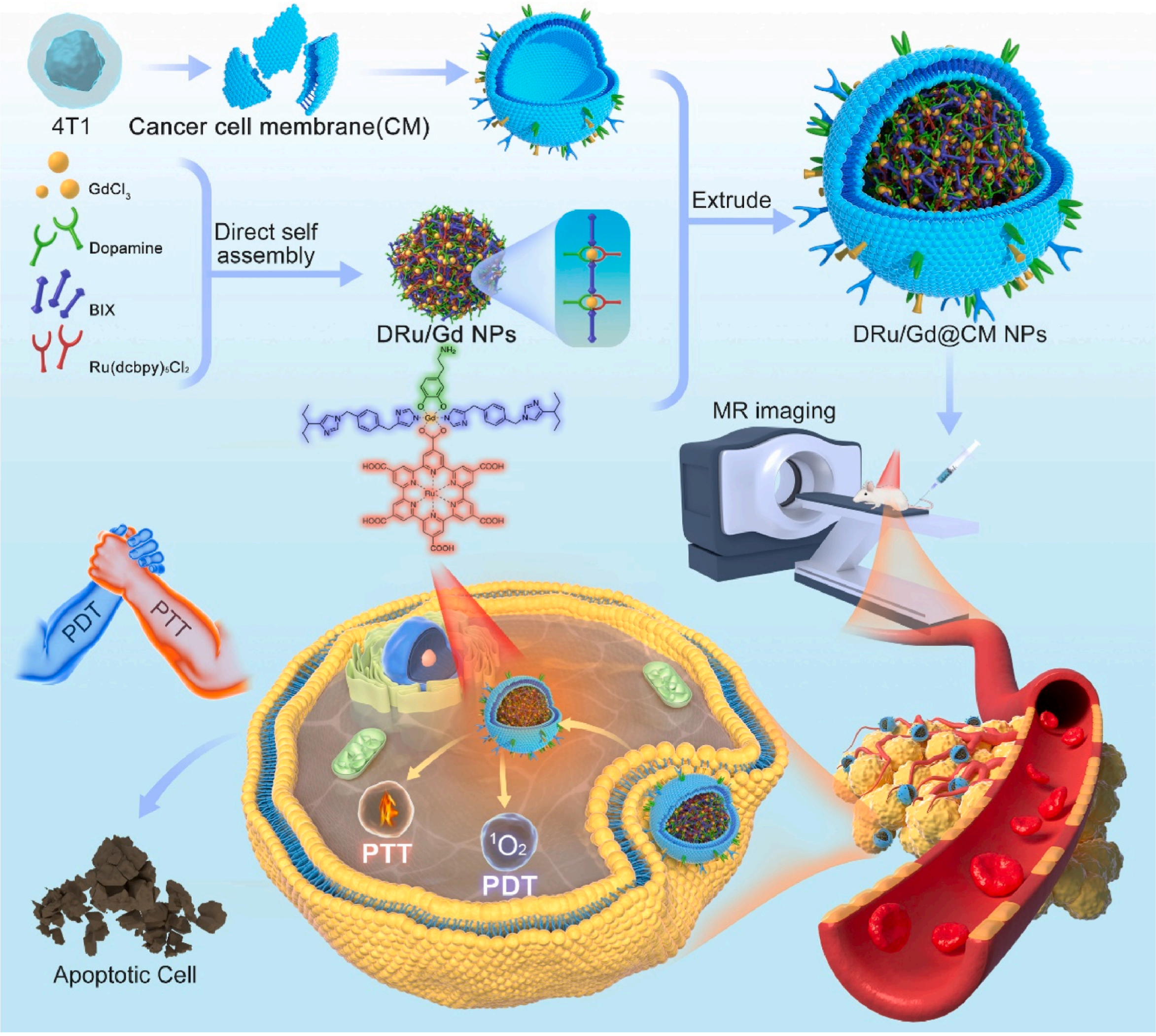

Scheme 1. The synthetic route of biomimetic nanodrugs (DRu/Gd@CM NPs) and its subsequent application in targeted phototherapy of mice subcutaneous breast cancer tumor model.

synthesized multifunctional nanoparticles retain the distinct attributes of each precursor, embodying the robust magnetic resonance feedback of gadolinium ions, the potent photodynamic prowess of ruthenium complexes, and the impressive photothermal attributes of dopamine. Conclusively, this nanoplatform was employed for magnetic resonance imaging-guided PDT/PTT interventions in tumor prototypes.

2. Experimental section

2.1. Materials

All chemicals and reagents were analytical grade and used without further purification. Dopamine hydrochloride (DA, 99.0%), 1,4-Bis[(1H-imidazole-1-yl)methyl]benzene (BIX) and 9,10-anthracenediyl-bis (methylene) dimalonic acid (ABDA) were purchased from Aladdin Chemistry Co. Ltd., Shanghai, China. Tris-(4,4′-dicarboxylic acid-2,2-bipyridyl)ruthenium(II) dichloride ($Ru(dcbpy)_3Cl_2$) was purchased from Shanghai Macklin Biochemical Technology Co., Ltd. (China). The Cell Counting Kit-8 (CCK-8) was obtained from GLPBIO, America. Gadolinium (III) chloride hexahydrate ($GdCl_3•6H_2O$, 99.99%) was purchased from Shanghai Meryer Chemical Technology Co., Ltd. The reactive oxygen species (ROS) assay kit 2′,7′-dichlorofluorescin diacetate (DCFH-DA) and Roswell Park Memorial Institute medium 1640 (RPMI-1640) were obtained from Solarbio Science & Technology Co., Ltd. (Beijing). Fetal bovine serum (FBS) was purchased from Zhejiang Tianhang Biotechnology Co., Ltd., China. Dimethylformamide (DMF) and other solvents were obtained from Zhiyuan Chemical Reagent Co., Ltd., Tianjin, China.

2.2. Characterization

Transmission electron microscopy (TEM) images were performed on a FEI Titan G260-300 microscope equipped with Super-X EDX detector system. Ultraviolet–visible spectroscopy (UV–Vis) was recorded using a UV-2700i spectrophotometer (Shimadzu, Japan). Dynamic light scattering (DLS) and Zeta potential were determined through Malvern Zetasizer Nano ZS90. X-ray photoelectron spectroscopy (XPS) was collected by Scientific K-Alpha (Thermo Scientific). X-ray diffraction (XRD) spectrum was collected by SmartLab SE (Rigaku, Japan). The content of gadolinium was detected by Inductively coupled plasma mass spectrometry (ICP-MS, PerkinElmer). Fourier transform infrared spectroscopy (FTIR) was acquired by Spectrum GX (Perkin-Elmer). Fluorescent spectrum was obtained by a Fluo-romax-4P spectrometer (Horiba).

2.3. Preparation of DRu/Gd NPs

The mixture of 95 mg Dopamine, 30 mg BIX, and 4 mg $Ru(dcbpy)_3Cl_2$ was dissolved in 15 mL of DMF solution. The solution was magnetically stirred at a speed of 900 rpm and heated to 100 °C. Add 44 mg $GdCl_3·6H_2O$ dissolved in 5 mL DMF drop by drop. Then, the reaction was sustained at 100 °C for 2 h. After that, the prepared nanoparticles were obtained by centrifugation at 8000 rpm and washed with anhydrous ethanol 3 times.

2.4. Preparation of CM fragments

4T1 cells were purchased from Cell Bank of Type Culture Collection of Chinese Academy of Sciences (Shanghai, China). Commonly, 4T1 cells were harvested and then resuspended in cold PBS. The collected cells were suspended in a hypotonic lysing buffer containing PMSF (Beyotime, China) and membrane protein extraction reagent. The 4T1 cells were incubated in ice bath for 15 min and then broken repeatedly using a freeze-thaw method. After centrifugation at 800 × *g* for 10 min, the supernatant was further centrifuged at 15,000 × *g* for 30 min to obtain the cell membrane fragments. The membrane products of CM-4T1 were lyophilized and stored at −80 °C. The lyophilized membranes are rehydrated in ultrapure water or PBS buffer.

2.5. Preparation of DRu/Gd@CM NPs

A successive extrusion approach was utilized to prepare the DRu/Gd@CM NPs. Briefly, 1 mL aqueous solution of DRu/Gd NPs with varied concentration (0.1, 0.2, 0.3, 0.4, or 0.5 mg/mL) was mixed with CM-4T1 dispersions (1 mL, 1.0 mg/mL). The DRu/Gd NPs and CM were transferred into a syringe and successively extruded through 800 nm, 400 nm, and 200 nm water-phase filters, followed by centrifugation to remove unloaded DRu/Gd NPs from the dispersions. Finally, a DRu/Gd@CM dispersion with encapsulated DRu/Gd NPs at a high concentration (200 μg/mL) was obtained for further structural characterization and measurements.

2.6. SDS-PAGE

To verify the successful coating of CM, the membrane proteins in CM was characterized by sodium dodecyl sulfate polyacrylamide gel electrophoresis (SDS-PAGE). DRu/Gd, CM-4T1 and DRu/Gd@CM samples were heated at 95 °C for 5 min in the SDS sample buffer. Samples and protein markers were then slowly added to the pores of the gels. Electrophoresis was carried out at a constant voltage of 100 V for 2 h. Then, a gel was dyed with Coomassie brilliant blue staining solution, incubated at room temperature for 2 h, dyed on a shaker for 90 min, and decolored overnight for photographic analysis. And the results successfully showed that DRu/Gd@CM had almost the same protein composition as the original CM-4T1. As far as gadolinium is concerned, inductively coupled plasma-mass spectroscopy (ICP-MS) data confirmed a total amount of 16.798% in the nanoparticles.

2.7. Detection of the ROS in vitro

ROS generation was determined by 9,10-anthracenyl-bi (methylene) dimalonic acid (ABDA) and DCFH assay, respectively. Specifically, 100 μL of DRu/Gd@CM NPs with different concentration gradients (0, 5, 10, 25, 50, 75, 100, 200 μg/mL) to each well (96-well plates) DCFH with a final concentration of 10 μmol/L. The experimental group was irradiated with near-infrared light (660 nm, 0.5 W/cm^2, 10 min), while the control group was not exposed to near-infrared light. Molecular Devices (SpectraMaxR i3X) were used to detect the fluorescence intensity at 0, 10, 20, 30, 40, 50, and 60 min respectively, using the excitation wavelength of 488 nm and the emission wavelength of 525 nm. For ABDA assay. DRu/Gd@CM NPs were mixed with ABDA, then the mixture was irradiated by a 660 nm laser. The absorption of ABDA at 378 nm was monitored for every 5 min.

2.8. Photothermal performance

The photothermal properties of DRu/Gd@CM NPs were determined using 808 nm near-infrared light. To investigate the concentration dependence of the photothermal effect, various concentrations of DRu/Gd@CM NPs in solution (0, 25, 50, 100, 200, and 400 μg/mL) were irradiated for 10 min. To investigate the light intensity of the photothermal effect, various light power (0, 0.5, 1, 1.5, 2, and 2.5 W/cm^2) were irradiated for 10 min at the concentration of 400 μg/mL of DRu/Gd@CM NPs in solution. The photothermal stability of DRu/Gd@CM NPs was evaluated by irradiated DRu/Gd@CM NPs solution (200 μg/mL) in 5 repeated cycles of 10 min irradiation ON and 10 min OFF at power densities of 1.5 W/cm^2.

2.9. MR imaging

For relaxation measurement, different concentrations of DRu/Gd@CM NPs (Gd: 0, 0.1, 0.2, 0.3, 0.4 mM) were placed in 2 mL

Eppendorf tubes for MR imaging using an MR imaging scanning device (GE Architect 3.0 T, America). The main MRI sequences included fast spin echo (FSE) T1WI (TR/TE = 500/15 ms, NSA = 3, FOV = 80 × 80 mm, section thickness = 1.0 mm, matrix = 228 × 290) and mixed inversion-recovery spin echo T1-mapping sequence (firstly with an inversion recovery pulse: TR/TE/TI = 4000/160/400 ms; then a spin echo pulse: TR/TE = 3500/20 ms, NSA = 1, FOV = 80 × 80 mm, section thickness = 1.0 mm, matrix = 512 × 512). Moreover, by measuring the longitudinal relaxation time (T1) and transverse relaxation time(T2) of DRu/Gd@CM NPs with different concentrations using a 3.0 T MR instrument, the longitudinal relaxation rate (r1) and transverse relaxation rate were calculated.

2.10. Cellular uptake

To study the uptake and targeting properties of DRu/Gd@CM NPs, we conducted three groups of experiments. 4T1, L929, MDA-MB-231 and RAW 264.7 cells were seeded in a laser confocal plate at a density of 5×10^4 cells per well and incubated at 37 °C for 24 h. Then remove the medium and add the designed NPs for 4 h, respectively. The cells were washed with PBS three times and stained the nucleus with Hoechst for 15 min. Finally, cell imaging was performed using fluorescence microscopy. Firstly, mouse cancer cell 4T1, normal cell L929 and MDA-MB-231 cells were selected to evaluate the ability to distinguish normal cells from tumor cells. Secondly, DRu/Gd NPs and DRu/Gd@CM NPs were co-cultured with 4T1 cells, respectively, to verify the homologous targeting of cancer cell membranes. Finally, to verify the immune escape of the cell membrane, DRu/Gd@CM NPs were co-cultured with Raw 264.7 cells.

2.11. Intracellular ROS generation

4T1 cells seeded in 6-well plates at a density of 2×10^5 cells per well and incubated at 37 °C for 24 h. The 6-well plates were randomly divided into five groups including (i) PBS, (ii) DRu/Gd@CM NPs (5 μg/mL), (iii) DRu/Gd@CM NPs (5 μg/mL) irradiated with 660 nm laser at 0.5 W/cm^2 for 10 min, (iv) DRu/Gd@CM NPs (50 μg/mL) irradiated with 660 nm laser at 0.5 W/cm^2 for 10 min. The cells in various groups were treated for another 4 h. The cells were incubated with 10 μM DCFH-DA for 30 min. Subsequently, the fluorescence images were acquired by fluorescence microscope.

2.12. In vitro cytotoxicity assays

4T1 cells (96-well plates) were cultured in complete culture medium (RPMI 1640 medium with 10% fetal bovine serum) at 37 °C and 5% CO_2. Interventions were initiated at 70% cell fusion. After 12 h, remove the cell culture medium and then treated the cells in different groups: (i) PBS group; (ii) DRu/Gd@CM group, DRu/Gd@CM NPs with different concentration gradients (0, 5, 10, 25, 50, 75, 100, 200 μg/mL); (iii) PDT group, DRu/Gd@CM NPs with different concentration gradients (0, 5, 10, 25, 50, 75, 100, 200 μg/mL), and then irradiated with 660 nm laser (0.5 W/cm^2, 10 min); (iv) PDT group, DRu/Gd@CM NPs with different concentration gradients (0, 5, 10, 25, 50, 75, 100, 200 μg/mL), and then irradiated with 808 nm laser (1.5 W/cm^2, 10 min); (v) PDT/PTT group, DRu/Gd@CM NPs with different concentration gradients (0, 5, 10, 25, 50, 75, 100, 200 μg/mL), irradiated with 660 nm laser (0.5 W/cm^2, 10 min), and then irradiated with 808 nm laser (1.5 W/cm^2, 10 min). The cell viabilities were tested by a typical CCK-8 assay. Molecular devices (SpectraMaxR i3X) were used to detect the OD value at the wavelength of 450 nm. For flow cytometry assessments, 4T1 cells were cultured in 6-well plates (2×10^5 cells per well) overnight. After various treatments, the proportions of apoptosis in each group were analyzed. Furthermore, cell viabilities were also visualized by CAM/PI staining.

2.13. Animal model

Female BALB/C mice (18–22 g) were feed at 25 °C and 55% of humidity in Experimental Animal Center of Zhengzhou University (Zhengzhou, China). All animal experiments were raised in accordance with the guidelines of the Regional Ethics Committee and the Care Regulations approved by The First Affiliated Hospital of Zhengzhou University (ZZU-LAC20230804). The 4T1 tumor model was established by subcutaneous injection of 5×10^6 cells in 100 μL PBS into the right shoulder of the mice. The tumor size and body weight were measured every two days.

2.14. In vivo MR imaging

First, tumor model mice were built by injecting 100 μL of 4T1 cells (5×10^6 cells/mL). After 7 days, the volume was 100 mm^3, and a GE Achitect 3.0 T MR scanner was employed to evaluate the *in vivo* MR imaging performance of DRu/Gd@CM NPs. Before injection, the T1-weighted MR imaging of the tumor site was recorded. Then, the mouse was injected with 100 μL of DRu/Gd@CM NPs solution (20 μmol Gd^{3+} per kg) via a tail vein. After 1, 2, 4, 8, and 24 h, the T1-weighted MR imaging was re-recorded.

2.15. In vivo biological distribution

After IR783 and the Ru/Gd@CM(IR783) nanoparticles were injected through the tail vein, photos were taken using a live small animal fluorescence imaging system at 1 h, 6 h, 12 h, 24 h, and 48 h, respectively. Then the mice were dissected, and the heart, liver, spleen, lung and kidney and tumor were collected and imaged using a fluorescence imaging system to observe the metabolism of the drug in the internal organs.

2.16. In vivo combination therapy

Anti-tumor experimental studies were performed with 4T1 tumor-bearing BALB/c mice. After the tumor size reached about 100 mm^3, the mice bearing 4T1 tumors were randomly divided into 5 groups (six mice per group) and treated with (i) PBS group; (ii) DRu/Gd@CM group, DRu/Gd@CM NPs with different concentration gradients (0, 5, 10, 25, 50, 75, 100, 200 μg/mL); (iii) PDT group, DRu/Gd@CM NPs with different concentration gradients and then irradiated with 660 nm laser (0.5 W/cm^2, 10 min); (iv) PDT group, DRu/Gd@CM NPs with different concentration gradients and then irradiated with 808 nm laser (1.5 W/cm^2, 10 min); (v) PDT/PTT group, DRu/Gd@CM NPs with different concentration gradients (0, 5, 10, 25, 50, 75, 100, 200 μg/mL), irradiated with 660 nm laser (0.5 W/cm^2, 10 min), and then irradiated with 808 nm laser (1.5 W/cm^2, 10 min). The mice were intravenously injected with the corresponding nanoparticles (20 μmol Gd^{3+} per kg). Eight hours after the injection, the tumors were irradiated by 660 nm or 808 nm laser. The temperature changes in tumor areas were recorded by a thermal camera. To monitor tumor progression, the tumor volume changes were measured, and the mice bodyweight was also recorded. After 14 days of treatments, the mice were sacrificed, and major organs and tumors were obtained for further H&E, TUNEL, Ki67, and TNF-α staining.

2.17. Statistical analysis

All statistical analyses were used GraphPad Prism. The results of statistical analysis were presented as mean ± SD. Statistical significance was calculated by one-way ANOVA analysis. The statistical significance was defined as $^*p < 0.05$; $^{**}p < 0.01$; $^{***}p < 0.001$.

3. Results and discussion

3.1. Synthesis and characterization of DRu/Gd NPs

DRu/Gd NPs were produced using a straightforward one-step metal chelation approach. Typically, these nanoparticles were derived from $GdCl_3$, tris(4,4′-dicarboxylic acid-2,2′-bipyridyl)ruthenium(II) dichloride ($Ru(dcbpy)_3Cl_2$), and dopamine hydrochloride, using the bidentate ligand 1,4-bis(imidazole-1-ylmethyl)benzene (BIX). After stirring continuously for 2 h at ambient temperature, the resulting dark precipitate was isolated using centrifugation and carefully rinsed with ethanol to remove unattached ligands. Subsequently, the morphology, composition, and properties of these nanoparticles were examined. TEM images (Fig. 1a) display DRu/Gd NPs with consistent sizes around 210 nm and excellent water dispersion. A closer view in Fig. 1b reveals their distinct hexagonal formation with polished borders. Concurrently, dynamic light scattering (DLS) indicates that the particle size distribution for DRu/Gd NPs ranges from 150 to 420 nm, with an average size close to 300 nm. This measurement is somewhat larger than the TEM observation, likely attributed to nanoparticle hydration (Fig. 1c).

To ensure the successful integration of the metallic elements Gd and Ru into the nanoparticle matrix, we employed energy dispersive spectrometry (EDS). Fig. 1d demonstrates that the elemental spectrum of the nanoparticles consists of C, N, O, Ru, and Gd, distributed uniformly within the nanostructure. A subsequent XPS assessment provided a detailed chemical and elemental profile for the DRu/Gd NPs, highlighting an abundance of C, O, N, Ru, and Gd (Fig. 1e). Detailed spectral analysis, such as C1s, N1s, and O1s, revealed diverse bonding scenarios, like C═C, C–C, C–O, C–N, and O–C–O (Fig. S1). Notably, the high-definition spectrum showcased peaks correlating with Ru 3p at 464.7 and 485.3 eV, and those connected to Gd 4d at 142.7 and 147.7 eV. These peaks solidify that both Gd and Ru are intertwined within the DRu/Gd NPs framework (Fig. 1f–g) [43]. Furthermore, the powder X-ray diffraction (XRD) pattern in Fig. 1h ascertained the synthesized

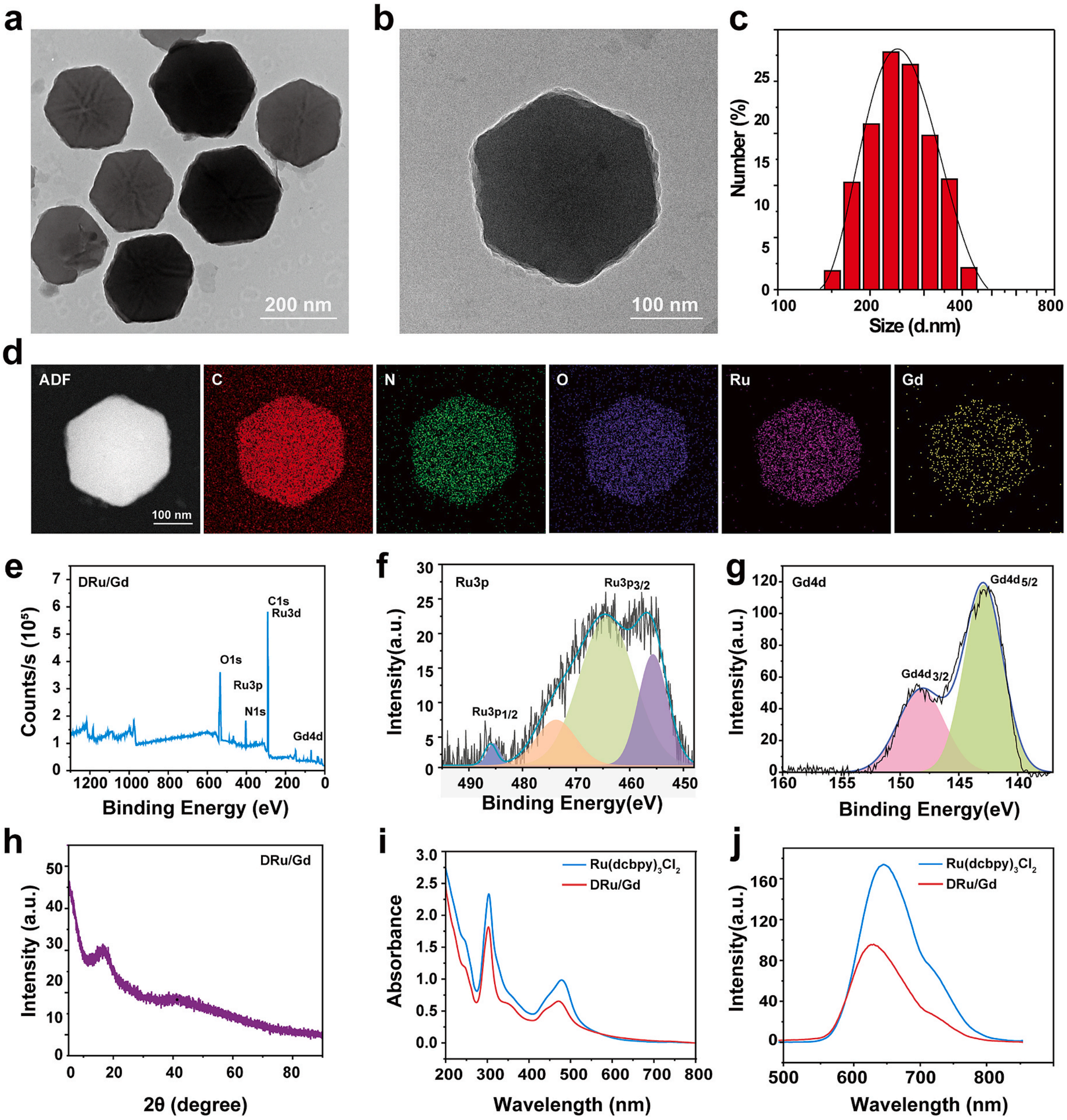

Fig. 1. (a, b) TEM images of DRu/Gd NPs with different magnifications; (c) The size distribution of DRu/Gd NPs; (d) EDS elemental maps of C, N, O, Ru and Gd distribution in DRu/Gd NPs; (e) XPS survey spectra of DRu/Gd NPs and the corresponding spectrums of (f) Ru3p and (g) Gd4d; (h) XRD spectra of DRu/Gd NPs; (i) UV–vis absorption of $Ru(dcbpy)_3Cl_2$ and DRu/Gd NPs; (j) Fluorescence spectrum of $Ru(dcbpy)_3Cl_2$ and DRu/Gd NPs.

nanocrystals possess a predominantly amorphous character [44]. Fourier transform infrared spectroscopy (FTIR) confirmed the presence of Ru, DA and a BIX ligand coordinated to the Gd(III) metal ions (Fig. S2). The FTIR spectrum shows the disappearance of the bands corresponding to the catechol –OH groups of DA in the range of ν = 3000-3500 cm^{-1}, reflecting their deprotonation, the stretching and bending vibrations of the amine group (3340 and 1618 cm^{-1}, respectively), and the stretching vibrations of C–H (3040 cm^{-1}) and C–C of the aromatic ring (1550 cm^{-1}). Moreover, the vibration band assigned to a C–O stretch for the catechol coordinated to the metal appeared in the frequency range 1200–1300 cm^{-1}. Additionally, typical vibrational bands of the BIX ligand (ν = 1520, 1262, 1105 cm^{-1}) were observed in the FT-IR spectra [45]. Concerning gadolinium, the inductively coupled plasma-mass spectroscopy (ICP-MS) results verified its presence at 16.8% within the nanoparticles. Next, the optical attributes of the DRu/Gd NPs were assessed and juxtaposed with those of $Ru(dcbpy)_3Cl_2$. As depicted in Fig. 1i, the UV–vis absorption of DRu/Gd NPs at 303 nm and 475 nm aligns closely with $Ru(dcbpy)_3Cl_2$ (304 nm and 479 nm), suggesting that the integration of $Ru(dcbpy)_3Cl_2$ has a negligible effect on these properties. Furthermore, the fluorescence emission patterns of DRu/Gd NPs mirror those of $Ru(dcbpy)_3Cl_2$, with both exhibiting a pronounced red fluorescence near 655 nm (Fig. 1j). These findings confirm the preservation of the red emission from $Ru(dcbpy)_3Cl_2$ in the nanoparticles, and that the coordination procedure doesn't compromise the DRu/Gd NPs' optical features.

3.2. *The synthesis and properties of DRu/Gd@CM NPs*

Subsequently, the cell membrane from breast cancer cell 4T1 was isolated (Fig. S3) and layered onto the nanoparticle surface via physical extrusion. An examination of the physicochemical attributes of DRu/Gd@CM NPs, before and after the cell membrane coating, was conducted. Fig. 2a–b highlight a discernible core-shell design for DRu/Gd@CM NPs and an uneven surface, signifying the presence of the cancer cell membrane. The protein composition of DRu/Gd@CM NPs was further analyzed by sodium dodecyl sulfate polyacrylamide gel electrophoresis (SDS-PAGE). The results showed that DRu/Gd@CM NPs had almost the same protein composition as the original 4T1 cell membrane (Fig. 2c), which further proved the success of cell membrane coating. DLS data revealed an increase in diameter from 252 nm for DRu/Gd NPs to 286 nm for DRu/Gd@CM NPs (Fig. S4). Concurrently, the zeta potential of DRu/Gd@CM NPs was clocked at −21.23 mV, resembling the potential of cancer cell membrane-derived vesicles (−23.5 mV) but markedly diverging from the DRu/Gd NPs (−8.79 mV)

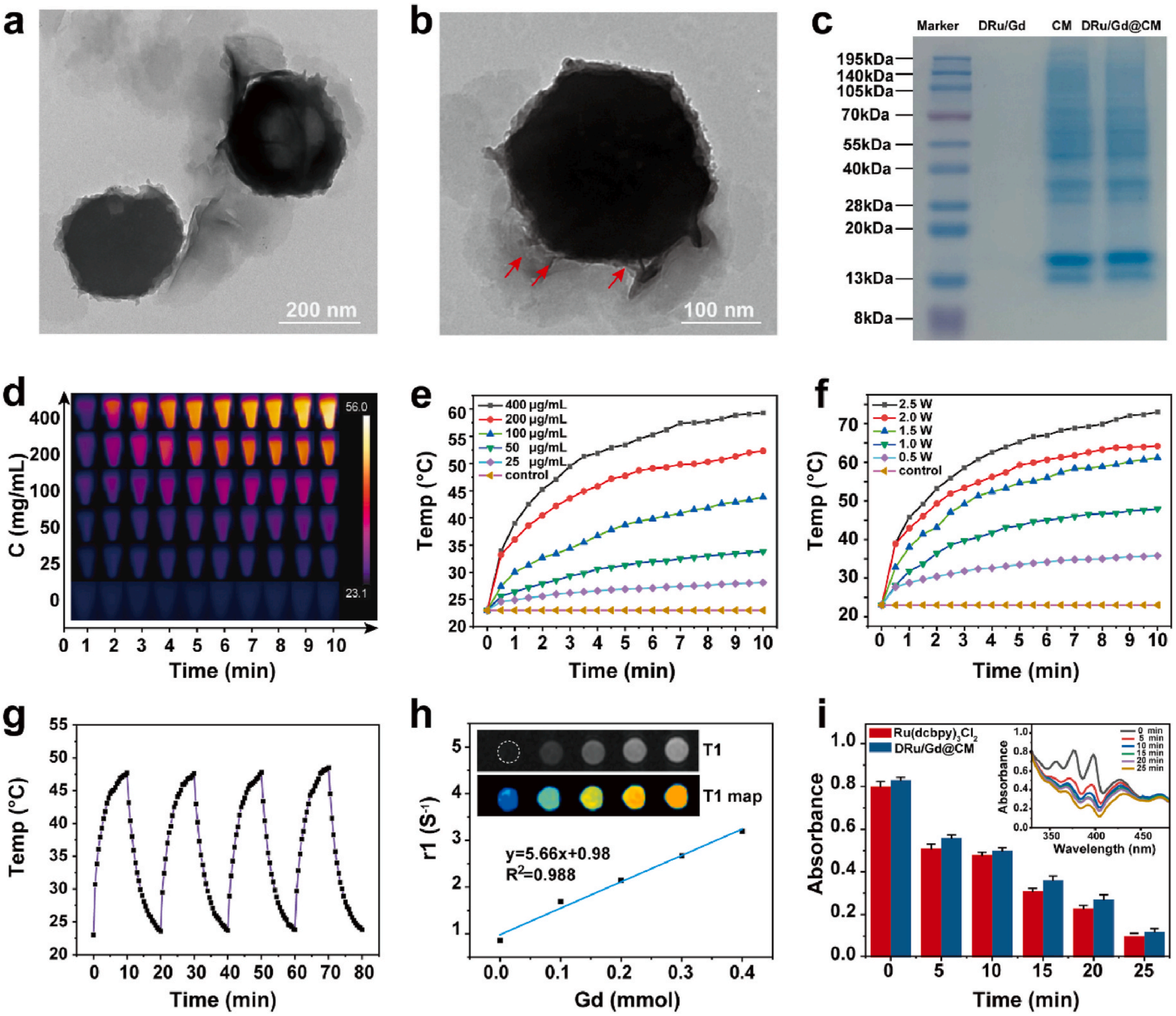

Fig. 2. (a, b) TEM image of DRu/Gd@CM NPs with different magnifications; (c) SDS-PAGE-based protein analyses of DRu/Gd@CM NPs, 4T1 cell membrane and DRu/Gd@CM NPs; (d) Thermal image of the solution with different concentration of DRu/Gd@CM NPs in 10 min; (e) Temperature curve of the solution with different concentration of DRu/Gd@CM NPs in 10 min; (f) Temperature curve of the DRu/Gd@CM NPs solution with different radiated power of in 10 min; (g) Temperature changes of DRu/Gd@CM NPs during five on/off cycles. (h) Longitudinal relaxivity r1 of DRu/Gd@CM NPs and the corresponding T1 and T1map images inserted; (i) The corresponding UV–vis absorption spectra of the mixture of ABDA and the DRu/Gd@CM NPs with different irradiation time periods.

(Fig. S5). Collectively, these observations attest to the successful coating of the cancer cell membrane on DRu/Gd NPs.

Dopamine, acting as a precursor molecule, undergoes autoxidative polymerization to generate polydopamine, equipping multifunctional nanoparticles with photothermal agents [46]. Consequently, the photothermal conversion attributes of DRu/Gd@CM NPs were scrutinized. Infrared thermal imagery and corresponding temperature graphs (Fig. 2d–e) show that DRu/Gd@CM NPs' temperatures vary based on concentration and exposure duration to laser. Specifically, after a 10-min laser exposure (1.5 W/cm^2), temperatures of DRu/Gd@CM NPs solutions surged, with peaks at 23.1, 28.1, 33.8, 42.6, 49.6, 59.3 °C for varying concentrations. Contrastingly, the equivalent volume of pure water under identical conditions saw a modest 1.8 °C increase. Moreover, the temperature dynamics of the DRu/Gd@CM NPs solution also exhibited dependence on laser power. Fig. 2f indicated that with apex temperature rises as the at power densities increased respectively. Additionally, DRu/Gd@CM NPs showcased steadfast photothermal conversion throughout four laser cycles (Fig. 2g), signifying impressive photothermal resilience without notable temperature drop-offs in the subsequent photothermal reactions.

MRI stands as a pivotal tool in disease diagnosis due to its non-invasiveness and high-resolution capabilities. Metal ion complexes, namely those involving manganese, gadolinium, and iron, have emerged as instrumental for MRI. However, these complexes grapple with a slew of challenges, such as pronounced toxicity, abbreviated half-life, and attenuated signal strength [47,48]. Addressing this, the conveyance of metal ions via DRu/Gd@CM NPs seeks to elevate the imaging efficacy of these metal complexes. As the concentration of Gd amplifies from 0.01 mM to 0.4 mM, there's a marked increase in the T1-weighted MRI signal intensity mediated by DRu/Gd@CM NPs. The longitudinal relaxivity coefficient (r1) registers at 5.66 mM^{-1} s^{-1} (Fig. 2h), which outstrips most of the hitherto reported T1-weighted contrast agents. Hence, this amalgamation of findings points to the potential of DRu/Gd@CM NPs acting as formidable CAs for T1-weighted MRI in tumor imaging.

Photodynamic therapy (PDT) has gained traction as a benign therapeutic modality to extirpate afflicted tissues via a photosensitive procedure. As shown in Fig. S6, the generation of singlet oxygen ($^1O_2$) by Ru-complexes has been ascertained by the electron spin resonance (ESR). Given that $^1O_2$ interacts with ABDA, causing a dip in its absorption at 378 nm, it's thus feasible to gauge $^1O_2$ generation. Upon amalgamating Ru(dcbpy)$_3$Cl$_2$ or the DRu/Gd@CM NPs (80 mM) with ABDA (100 mM) and subsequently subjecting them to 660 laser exposure (0.5 W/cm^2), there's a conspicuous reduction in absorption of 88.6% for Ru(dcbpy)$_3$Cl$_2$ and 91.1% for the DRu/Gd@CM NPs, all within a span of 25 min (Fig. 2i). These observations underscore the formidable $^1O_2$ generation prowess of DRu/Gd@CM NPs, which stems from the ligand, Ru(dcbpy)$_3$Cl$_2$. In stark contrast, the control samples exhibited tenacious stability under analogous conditions (Fig. S7). Moreover, when subjected to 660 nm laser irradiation, the fluorescence intensity of the solution amalgamating DRu/Gd@CM NPs and DCFH, illuminated at 525 nm, considerably surpasses its non-irradiated counterpart. This disparity is both concentration and time-sensitive (as seen inFig. S8). Such revelations reinforce the premise that DRu/Gd@CM NPs are adept at generating $^1O_2$, thereby accentuating their potential in photodynamic therapy.

3.3. Cell uptake and in vitro anticancer performance

A salient property of tumor cells is their homologous targeting, which is primarily predicated on the specific protein displayed on the cancer cells. Empirical research has indicated that nanoparticles camouflaged with cancer cell membranes can modify the cellular uptake dynamics. Western blot analysis was performed to confirm the cell adhesion molecules (EpCAM, galectin-3, and CD-47) expressed by 4T1 tumor cells, which is relevant for homotypic targeting and reduction of uptake by macrophages, thus realizing the specific recognition and binding of CM coated nanoparticles and cancer cells (Fig. S9). The effective internalization of therapeutic nanoparticles into tumor cells is paramount to achieving a robust therapeutic outcome. From the data presented in Fig. S10, it's evident that 4T1 cells rapidly internalize the DRu/Gd@CM NPs, with the fluorescence intensity inside the cells showing an incremental pattern over the span of 4 h.

To investigate the specificity of DRu/Gd@CM NPs to homologous 4T1 cells, the targeting capability of DRu/Gd@CM NPs to 4T1 cells, L929 and MDA-MB-231 cells were verified by CLSM. The results showed that the 4T1 group had the highest uptake efficiency and fluorescence intensity, demonstrating the specific binding ability of DRu/Gd@CM NPs to homologous 4T1 cells (Fig. 3a&3b). Further experimentation, where both DRu/Gd NPs and DRu/Gd@CM NPs were co-cultured with 4T1 cells as depicted in Fig. S11. Using laser confocal microscopy as a tool, it was discerned that nanoparticles encapsulated within cell membranes exhibit superior internalization by the 4T1 cells, thus signifying their inherent targeting capabilities. A significant advantage of biomimetic nanomaterials, especially those encapsulated with tumor cell membranes, lies in their capacity to evade macrophage clearance, thereby ensuring optimal accumulation in tumor tissues. In experiments that incubated macrophage-like RAW 264.7 cells with both DRu/Gd NPs and DRu/Gd@CM NPs, confocal laser scanning microscopy (CLSM) observations (Fig. S12) indicated a palpably diminished fluorescence intensity in the DRu/Gd@CM NPs cultured cells when compared to the DRu/Gd NPs. This substantiates the premise that a cancer cell membrane coat can markedly attenuate immune clearance. To further probe the reactive oxygen species (ROS) generating potential of DRu/Gd@CM NPs within cancer cells, Ru/Gd NPs were incubated with the probe 2′, 7′-dichlorodihydrofluorescein diacetate (DCFH-DA). As elucidated in Fig. 3c&d, 4T1 cells treated with DRu/Gd@CM NPs and DCFH-DA manifested pronounced green fluorescence under 660 nm laser exposure, with the fluorescence intensifying in a concentration-dependent manner. Contrarily, the control group exhibited negligible green fluorescence signals, underscoring the fact that DRu/Gd@CM NPs can potentiate ROS production post-irradiation within cancer cells.

To assess and compare the *in vitro* cytotoxicity of PDT effect of Ru-complex and, PTT effect arisen from PDAs, CCK-8 assay was performed. 4T1 cells were cultured with DRu/Gd@CM NPs, and radiated by NIR laser (660 nm with 0.5 W/cm^2, 808 nm with 1.5 W/cm^2 or 660/808 nm with 0.5 W/cm^2 and 1.5 W/cm^2, respectively) for 10 min. Fig. 3e indicates that treating the cancer cells with DRu/Gd@CM NPs concentrations between 0 and 200 μg/mL showed no notable cytotoxicity in the case of no irradiation, highlighting the biocompatibility of the nanoparticles. On the contrary, cells subject to NIR irradiation feature a positively dose-dependent cytotoxicity. DRu/Gd@CM NPs treated by the combined NIR laser irradiation (PDT/PTT: 660/808 nm) display the highest cytotoxicity. Especially, the cell viability is 28.3% for DRu/Gd@CM NPs treated group after the combined PDT/PTT treatment. While it is 47.9% or 41.8% for DRu/Gd@CM NPs treated group receiving PDT or PTT alone. Collectively, these results clearly displayed that DRu/Gd@CM NPs maintained both photothermal and photodynamic functions and they showed combined effect of PTT and PDT against tumor cells. The therapeutic efficacy against tumor cells by PDT/PTT was further confirmed by fluorescent staining of live/dead cells (Fig. 3f&g). The 4T1 cells were then stained with FITC/PI to verify that cell death occurred via the apoptotic pathway, i.e., programmed cell death. It is widely believed that Annexin V binds to exposed phosphatidylserine on the cell surface, especially in early apoptosis. As shown in Fig. 3h, the groups of Control, DRu/Gd@CM, PDT, and PTT all induced evident apoptosis in 4T1 cells (6.6 %, 11.31 %, 60.1 %, 72.23 %) which was much weaker than the dual laser-induced apoptosis (89.25 %) in DRu/Gd@CM NPs (PDT + PTT group). This significant difference is mainly attributed to the excellent optical therapy capability of DRu/Gd@CM NPs, including PTT and PDT. Notably, the apoptotic fraction of treatment with PDT or PTT alone is lesser than the PDT/PTT group, showcasing the synergistic potency of both PTT and PDT.

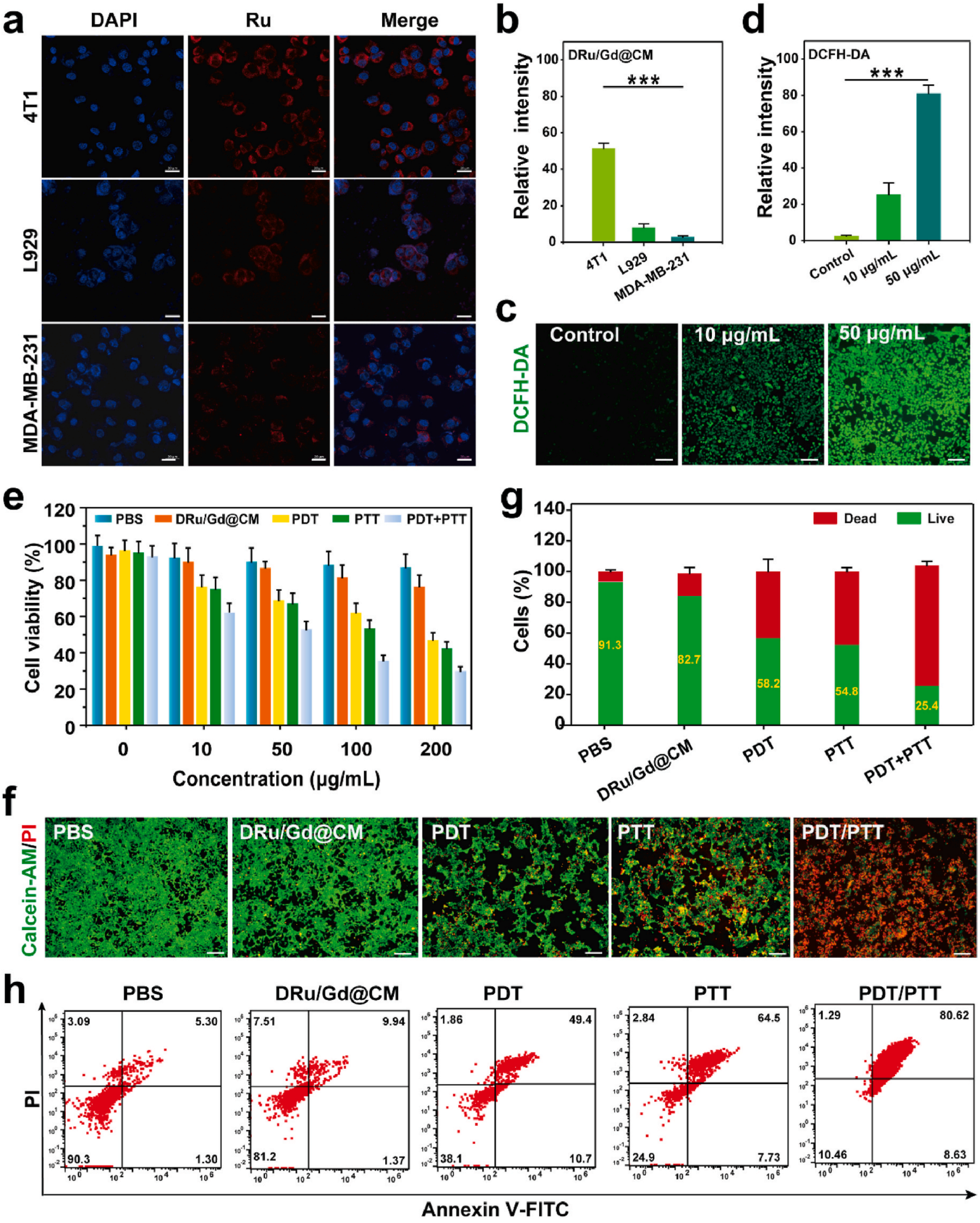

Fig. 3. (a) Fluorescence images of uptake from L929, MDA-MB-231 and 4T1 cells against DRu/Gd@CM NPs, scale bar: 10 μm; (b)Semi-quantitative analysis indicated targeting for 4T1 cells; (c) CLSM images of intracellular ROS generation from intact 4T1 cells with 660 nm photoirradiation (0.5 W/cm^2) in different concentrations (scale bar: 100 μm); (d) Related of fluorescent semi-quantitative analysis of DCFH; (e) The cell viability of 4T1 cells after incubation with a series concentration of DRu/Gd@CM accompanied with different treatments, PDT: irradiated with 660 nm laser, PTT: irradiated with 808 nm laser; (g) Quantification bar plots for live/dead staining; (f) Live/death staining of 4T1 cells after treated with PBS, DRu/Gd@CM, PDT, PTT, and PDT + PTT, Scale bar: 100 μm; (h) Flow cytometry assay of 4T1 cells after being incubated with different group for 24 h.

In order to investigate the tumor-targeting behavior of the proposed nanoplatform, the *in vivo* distribution of DRu/Gd@CM was further evaluated in a 4T1-bearing nude mice model. Considering that the quenching effect of PDA on fluorescent ruthenium complexes may affect the imaging effect, we tagged the DRu/Gd@CM NPs with the near-infrared dye IR783 for *in vivo* tracking. As shown in Fig. 4a, 12 h post-injection, the fluorescence signal in the free IR783 group noticeably dwindled, suggesting rapid body clearance of unbound IR783. Concurrently, DRu/Gd@CM/IR783 NPs exhibited a preferential tumor accumulation, peaking in fluorescence intensity at the 6-h mark. Remarkably, the tumor fluorescence intensities of the DRu/Gd@CM/IR783 NPs were obviously stronger than that of free IR783 in different

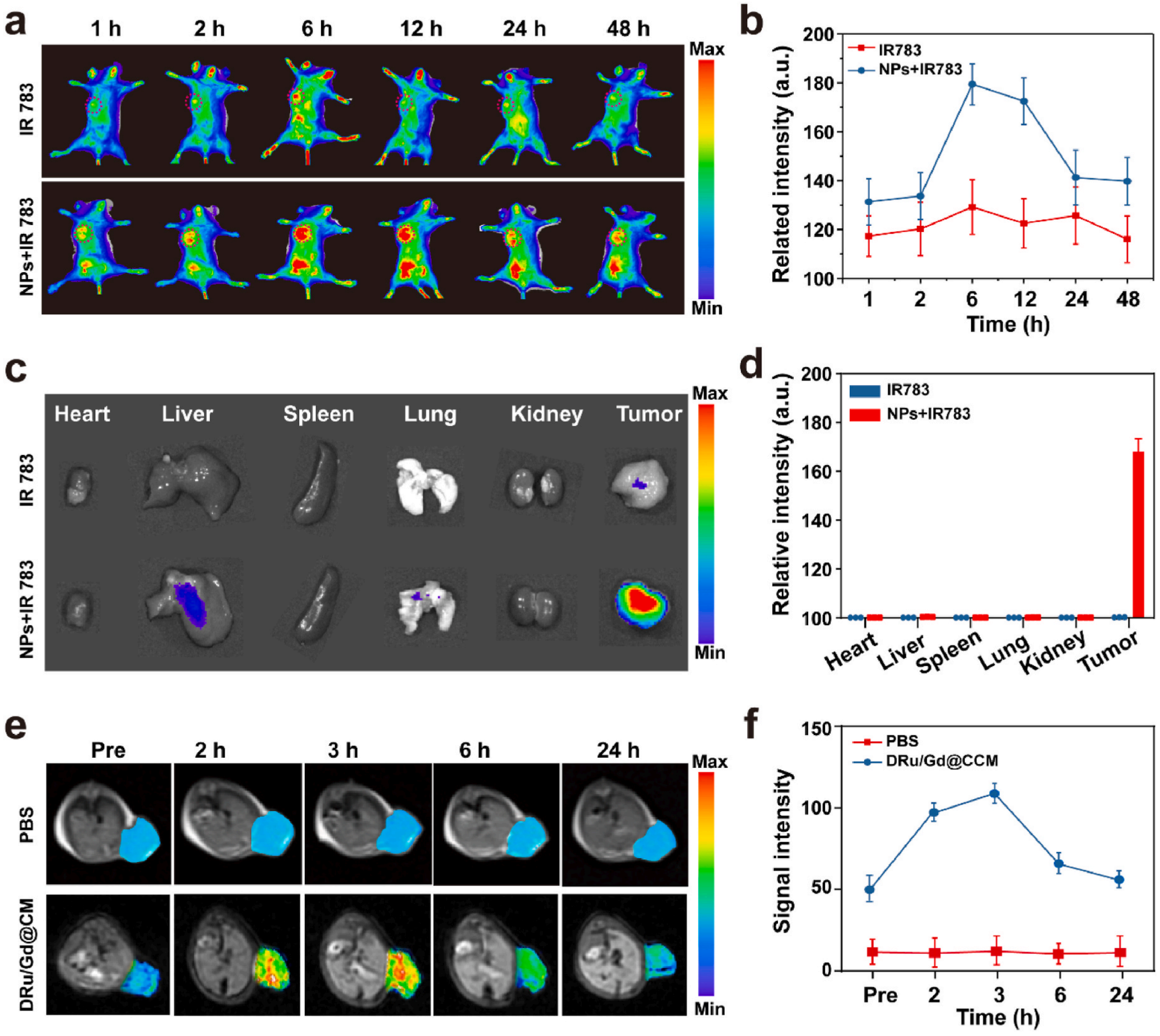

Fig. 4. (a) Time-dependent fluorescence imaging of 4T1-Balb/c mice intravenously injected with the DRu/Gd@CM NPs; (b) Quantification of the fluorescence trends of the corresponding treatment; (c) *Ex-vivo* NIR fluorescence images and (d) related intensity of IR783 in the harvested organs (heart, liver, spleen, lung, kidney) and tumors at 48 h post-administration (n = 3); (e) T1-weighted MR images of mouse Balb/c 4T1 breast cancer in axial and (f) MR signal intensity of tumors before and post the intravenous injection of DRu/Gd@CM NPs.

time points. Moreover, the fluorescence persisted even after 48 h, indicating sustained retention within the tumor (Fig. 4b). Furthermore, the fluorescent images of heart, liver, spleen, lung, kidneys, and tumor were recorded for capturing the distributions of DRu/Gd@CM in these major organs so as to precisely assess their tumor targeting. Fig. 4c exhibits that almost no fluorescence was detected in the major organs and tumors of the free IR 783, suggesting IR 783 was removed from the body after 48 h injection. In the DRu/Gd@CM/IR783 NPs groups, fluorescence appeared in the liver and tumor, while the group of DRu/Gd@CM/IR783 presented the strongest signal in tumors at 48 h (Fig. 4d).

Given the decent r1 relaxivity and the good cytocompatibility, the feasibility of Gd-doped nanoparticles as MR T1 contrast agents for tumor imaging was investigated. DRu/Gd@CM NPs was intravenously administered into a tumor-bearing mouse to further evaluate its targeting MRI capacity *in vivo* with 3.0 T MR scanner. The mouse with subcutaneous tumor was imaged pre- and post-injection of DRu/Gd@CM NPs and the obtained MR images are presented in Fig. 4e. Compared to the pre-injection MR image, a marked enhancement in the tumor region at 3 h post-injection of DRu/Gd@CM NPs is evidenced and the enhanced MR contrast lasts at least for 9 h, confirming that the DRu/Gd@CM NPs can accumulate in the tumor region (Fig. 4f). Such results demonstrate that a large amount of DRu/Gd@CM NPs accumulates in the tumor owing to the active targeting ability of the cancer cell membrane and the enhanced permeability and retention (EPR) effect occurring in the vessels of the cancer tissues. Importantly, the enhancement of the MRI signals in the tumor is capable of continuing for 24 h, which provides adequate time for guiding the following treatment.

3.4. *In vivo anti-tumor therapy*

Motivated by the promising antitumor effects of DRu/Gd@CM NPs *in vitro*, we further investigated their therapeutic efficacy *in vivo*. The performance of DRu/Gd@CM was tested on 4T1 tumor-bearing BALB/c mice. Once the primary tumor volume reached approximately 80 mm^3, mice were grouped randomly (n = 6) and treated with PBS, DRu/Gd@CM, PDT, PTT, and PDT + PTT as depicted in Fig. 5a. To begin, we evaluated the *in vivo* photothermal properties, as illustrated in Fig. 5b. When subjected to 808 nm laser (1.5 W/cm^2) for 10 min, the tumor temperature in the PTT group soared to 53 °C. In contrast, the control group showed negligible change, underscoring the potent photothermal effects of DRu/Gd@CM NPs (Fig. 5c). Using calipers, tumor volumes were recorded, with the growth curves depicted in Fig. 5d. Notably, Fig. 5e demonstrated the treatment outcomes across groups over a 14-

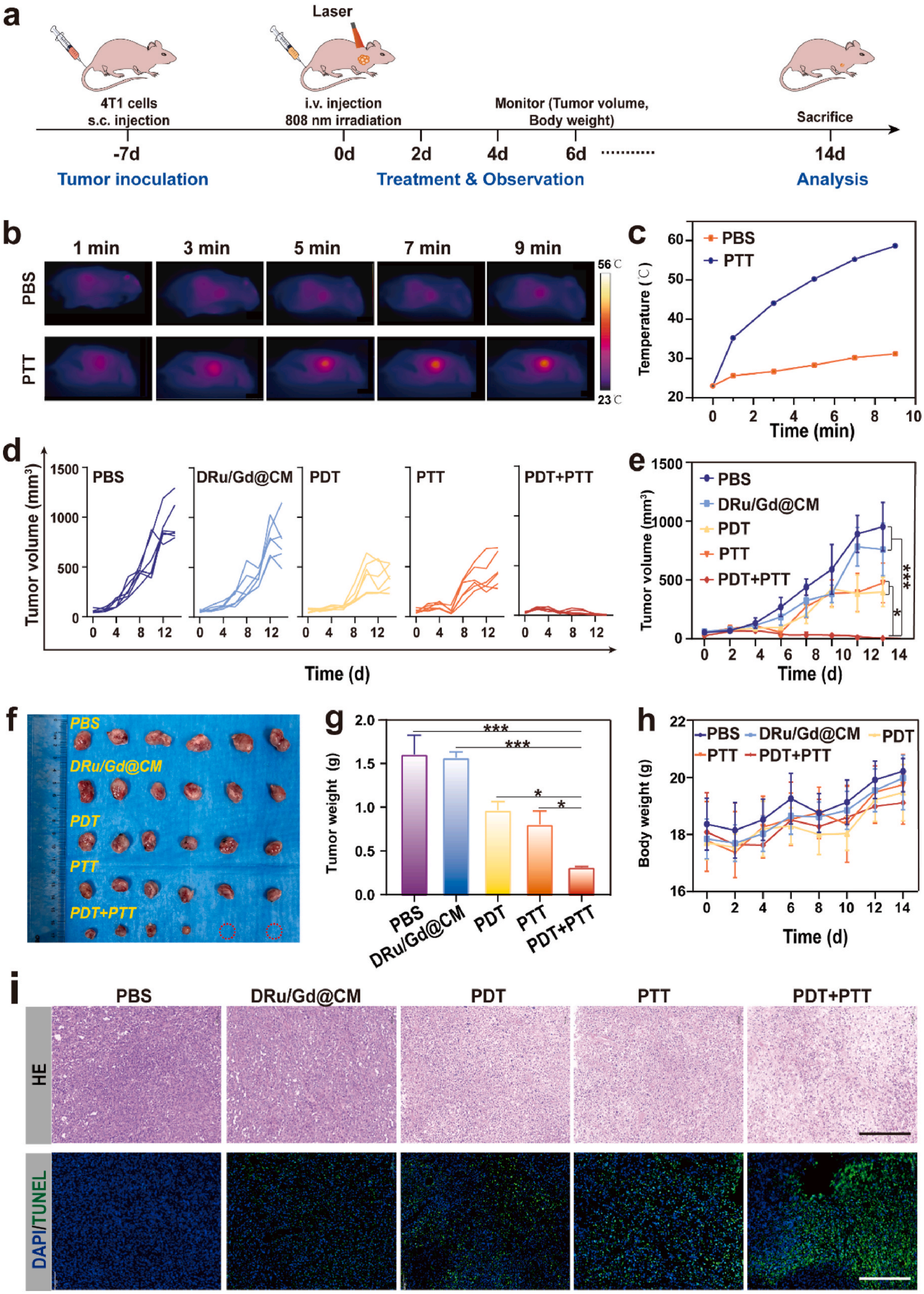

Fig. 5. The therapeutic effect of the DRu/Gd@CM NPs on 4T1 tumor model mice. (a) Schematic diagram of the treatment process of tumor-bearing model mice with PDT/PTT; (b) Infrared thermal images and (c) temperature change at the tumor sites of mice bearing 4T1 tumors treated with injection of PBS and DRu/Gd@CM NPs followed by 808-nm laser irradiation (1.5 W/cm^2, 10 min). (d, e) tumor volume changes of different groups in 14 days; (f) morphology and (g) tumor weight at the 14 days recorded in different groups; (h) body weight changes of Balb/c mice of different groups; (i) H&E and TUNEL stained images of the tumors from different groups on day 14 (scale bar: 200 μm, n = 3).

day period. The PDT + PTT group, in comparison to PBS and other groups, exhibited remarkable tumor growth inhibition. This antitumor effect became even more apparent when examining the excised tumors after the 14-day treatment window (Fig. 5f). The tumors, post-study, were also weighed (Fig. 5g), corroborating the earlier observations. Throughout the treatment duration, mice body weight remained relatively stable across groups (Fig. 5h). Besides, histological analysis including H&E and Tunel staining of tumor tissues showed the typical histomorphological structures and apoptosis in tumors (Fig. 5i), which were corresponding to the above results in different groups. These outcomes declared that the PDT/PTT combined tumor therapy by DRu/Gd@CM NPs could efficiently inhibit the tumor growth.

The antitumor mechanism of DRu/Gd@CM NPs under irradiation was explicitly researched for deeply digging into how it fulfilled such an effective tumor-inhibitory efficacy. Immunofluorescence staining of the proliferation cell biomarker, Ki-67, was carried out to evaluate the cancer cells proliferation rate in different groups, 14 days after treatment. This biomarker is commonly used in the clinic for identifying the prognosis and effectiveness of treatment in patients [49]. According to the immunofluorescence analyses (Fig. 6a) and their corresponding quantitative values (Fig. 6b), the percentages of the tumor cells that were positive for the Ki-67 biomarker were 78.4 ± 5.6%, 66.8 ± 4.2%, 41.2 ± 4.5%, 31.2 ± 3.8%, and 5.9 ± 3.1% for the control, DRu/Gd@CM, PDT, PTT, and PDT + PTT groups, respectively. Therefore, the PDT + PTT group with a lower percentage of Ki-67-positive tumor cells could effectively control proliferation compared with the other groups. As a representative cytokine of cellular immunity, the serum tumor necrosis factor TNF-α, plays an important role in tumor immunotherapy [50]. To further analyze the immune mechanism of PDT + PTT on tumor inhibition, we detected the expression of immune cytokine TNF-α. As expected, PDT + PTT treatment could effectively promote the expression of immune cytokine TNF-α (Fig. 6c). This was ascribed to that PDT and PTT are immunogenic cell death (ICD) inducers via stimulating necrotic cells release damaged associated molecular patterns (DAMPs), triggering the production of TNF-α. Therefore, this result further indicates that the combination of PDT and PTT can effectively activate anti-tumor immune response and inhibit the growth of tumor cells.

Then, histological analysis of the major organs (heart, lung, liver, spleen, and kidney) harvested from mice post DRu/Gd@CM NPs assisted PDT, PTT or PDT/PTT treatment were also carried out by staining to

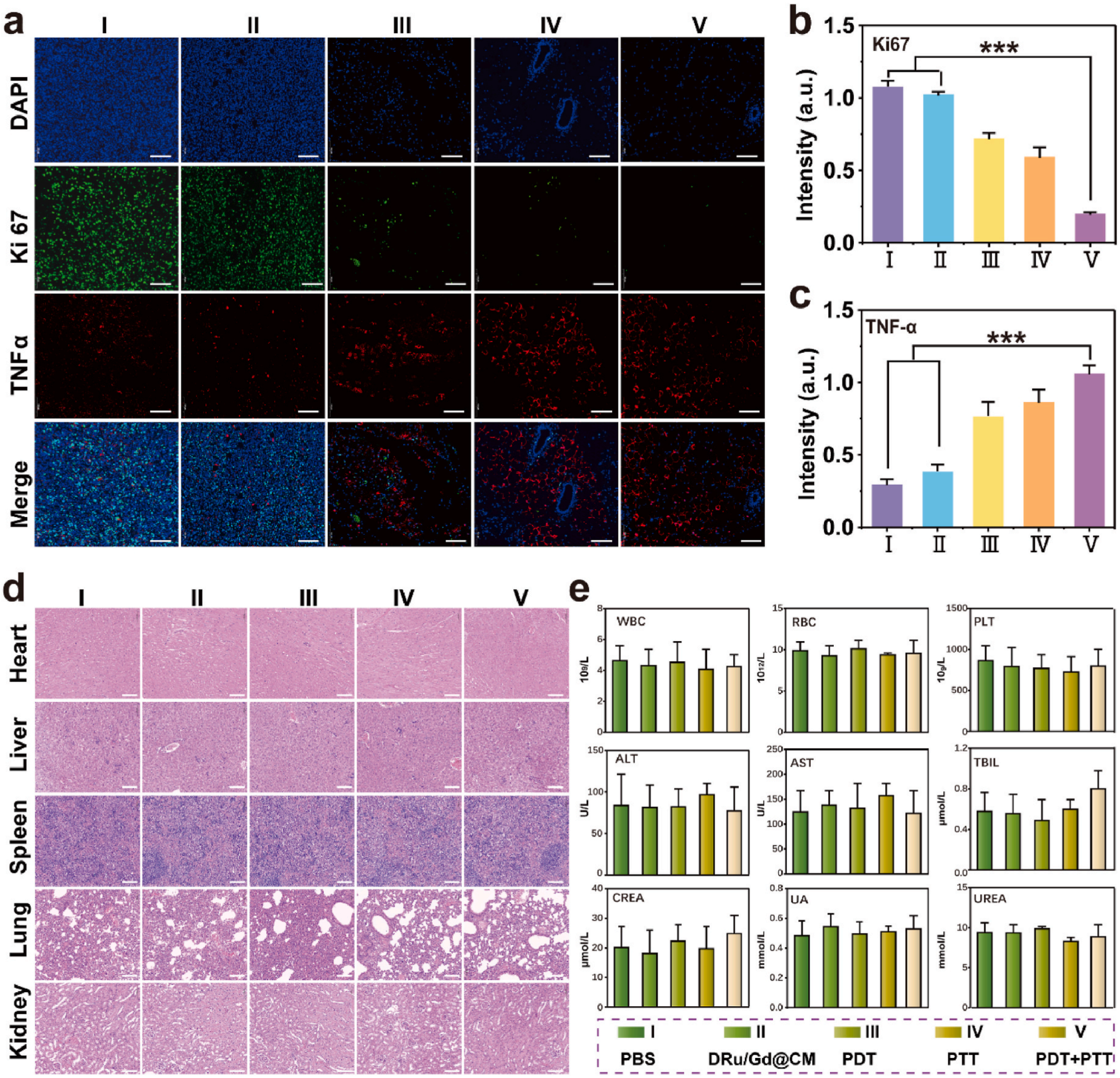

Fig. 6. (a) Ki67 and TNF-α stained images of the tumors from different groups on day 15 (scale bar: 100 μm, n = 3); Quantification of the fluorescence intensity of (b) Ki67 and (c) TNF-α of the corresponding images; (d) H&E histological staining of main organs after intravenous injection of different drug formulations. Scale bar = 100 μm; (e) Blood biochemistry and hematology analysis of mice after different treatments.

assess their *in vivo* cytotoxicity. Fig. 6d shows representative pictures of these organs at different time intervals. Compared to the images from control group, no apparent histological abnormalities or inflammation lesions could be seen in all these organs from mice treated with DRu/Gd@CM NPs assisted PDT, PTT or PDT/PTT treatment, thus giving solid evidence to their positive biocompatibility *in vivo*. To estimate the potential cytotoxicity to the body post PTT/PDT combined treatment, a hematology study was carried out. As shown Fig. 6e, no discernible pathological abnormalities in blood index were observed in all groups. Collectively, these results suggest that the combined PTT and PDT mediated by DRu/Gd@CM NPs offers an optimal *in vivo* therapeutic approach for treating solid tumors.

4. Conclusion

In summary, we successfully synthesized a multifunctional nanoplatform camouflaged with a cancer cell membrane, termed DRu/Gd@CM, through a multifaceted approach. This novel construct facilitates magnetic resonance imaging-guided combined photothermal and photodynamic tumor therapies. The morphology of these structures can be fine-tuned by varying precursor ratios. Encouragingly, inherent traits of these precursors, such as PDA's photothermal attributes, magnetic resonance (MR) responsiveness of gadolinium ions, and the singlet oxygen production capacity of Ru(dcbpy)$_3$Cl$_2$, remain intact within these combined metal nanoparticles. *In vitro* studies revealed that nanoparticles encapsulated with homologous cell membranes demonstrated enhanced 4T1 cell internalization and superior immune evasion when compared to their coordinated counterparts. *In vivo*, this multifunctional structure emitted vibrant MRI signals and exhibited both photothermal and photodynamic therapeutic actions. This culminated in the efficient curtailment of tumor growth, even leading to complete tumor eradication within a 21-day window. This successful creation of biomimetic bimetallic coordinated nanoplatforms, achieved via a multi-pronged approach for significant advancements in the amalgamation of multiple modules within theranostics. Such developments hold promising implications for future innovations in bioimaging, biomedicine, and related domains.

CRediT authorship contribution statement

Mengyang Zhou: Writing – original draft, Data curation. **Yifei Wang:** Writing – review & editing, Funding acquisition, Formal analysis. **Yaning Xia:** Software, Methodology, Formal analysis. **Yinhua Li:** Software, Methodology. **Jianfeng Bao:** Software, Investigation, Data curation. **Yong Zhang:** Writing – review & editing, Project administration. **Jingliang Cheng:** Supervision, Project administration, Conceptualization. **Yupeng Shi:** Writing – review & editing, Supervision, Funding acquisition.

Declaration of competing interest

The authors declare that they have no known competing financial interests or personal relationships that could have appeared to influence the work reported in this paper.

Data availability

Data will be made available on request.

Acknowledgments

This work was financially supported by the National Natural Science Foundation of China (No. 81901808, 82303779), Henan Provincial Natural Science Foundation (232300420041) and the Project of Henan Provincial Medical Science and Technology Research Plan (No. SBGJ202002086, LHGJ20230177).

Appendix A. Supplementary data

Supplementary data to this article can be found online at https://doi.org/10.1016/j.mtbio.2024.101019.

References

[1] S.H. Yun, S.J.J. Kwok, Light in diagnosis, therapy and surgery, Nat. Biomed. Eng. 1 (1) (2017) 1–16.
[2] E.S. Shibu, M. Hamada, N. Murase, V. Biju, Nanomaterials formulations for photothermal and photodynamic therapy of cancer, J. Photoch. and Photobio. C. 15 (2013) 53–72.
[3] Y. Sun, Y.F. Zhang, Y. Gao, P. Wang, G. He, N.T. Blum, J. Lin, Q.H. Liu, X.B. Wang, P. Huang, Six birds with one stone: versatile nanoporphyrin for single-laser-triggered synergistic phototheranostics and robust immune activation, Adv. Mater. 32 (48) (2020) 2070360.
[4] J.H. Correia, J.A. Rodrigues, S. Pimenta, T. Dong, Z. Yang, Photodynamic therapy review: principles, photosensitizers, applications, and future directions, Pharmaceutics 13 (9) (2021) 1332.
[5] W. Wang, C. Chen, Y. Ying, S. Lv, Y. Wang, X. Zhang, Z. Cai, W. Gu, Z. Li, G. Jiang, F. Gao, Smart PdH@MnO$_2$ yolk-shell nanostructures for spatiotemporally synchronous targeted hydrogen delivery and oxygen-elevated phototherapy of melanoma, ACS Nano 16 (4) (2022) 5597–5614.
[6] J.L. Xie, Y.W. Wang, W. Choi, P. Jangili, Y.Q. Ge, Y. Xu, J.L. Kang, L.P. Liu, B. Zhang, Z.J. Xie, J. He, N. Xie, G.H. Nie, H. Zhang, J.S. Kim, Overcoming barriers in photodynamic therapy harnessing nano-formulation strategies, Chem. Soc. Rev. 50 (16) (2021) 9152–9201.
[7] M.H. Lan, S.J. Zhao, W.M. Liu, C.S. Lee, W.J. Zhang, P.F. Wang, Photosensitizers for photodynamic therapy, Adv. Health. Mat. 8 (13) (2019) 1900132.
[8] J. Karges, M. Tharaud, G. Gasser, Polymeric encapsulation of a Ru(II)-Based photosensitizer for folate-targeted photodynamic therapy of drug resistant cancers, J. Med. Chem. 64 (8) (2021) 4612–4622.
[9] J. Karges, J. Li, L.L. Zeng, H. Chao, G. Gasser, Polymeric encapsulation of a ruthenium polypyridine complex for tumor targeted one- and two-photon photodynamic therapy, ACS Appl. Mater. Interfaces 12 (49) (2020) 54433–54444.
[10] K. Yang, S.J. Zhao, B.L. Li, B.H. Wang, M.H. Lan, X.Z. Song, Low temperature photothermal therapy: advances and perspectives, Coord. Chem. Rev. 454 (2022) 214330.
[11] J.Q. Chen, C.Y. Ning, Z.N. Zhou, P. Yu, Y. Zhu, G.X. Tan, C.B. Mao, Nanomaterials as photothermal therapeutic agents, Prog. Mater. Sci. 99 (2019) 1–26.
[12] S. Liu, X.T. Pan, H.Y. Liu, Two-dimensional nanomaterials for photothermal therapy, Angew. Chem. Int. Ed. Engl. 59 (15) (2020) 5890–5900.
[13] G. Gao, X.B. Sun, G.L. Liang, Nanoagent-promoted mild-temperature photothermal therapy for cancer treatment, Adv. Funct. Mater. 31 (25) (2021).
[14] J.D. Shao, C.S. Ruan, H.H. Xie, Z.B. Li, H.Y. Wang, P.K. Chu, X.F. Yu, Black-phosphorus-incorporated hydrogel as a sprayable and biodegradable photothermal platform for postsurgical treatment of cancer, Adv. Sci. 5 (5) (2018) 1700848.
[15] S.G. Wang, X. Li, Y. Chen, X.J. Cai, H.L. Yao, W. Gao, Y.Y. Zheng, X. An, J.L. Shi, H. R. Chen, A facile one-pot synthesis of a two-dimensional MoS$_2$Bi$_2$S$_3$ composite theranostic nanosystem for multi-modality tumor imaging and therapy, Adv. Mater. 27 (17) (2015) 2775–2782.
[16] Z.Q. Lv, S.J. He, Y.F. Wang, X.Y. Zhu, Noble metal nanomaterials for NIR-triggered photothermal therapy in cancer, Adv. Healthcare Mater. 10 (6) (2021) 2001806.
[17] M. Overchuk, R.A. Weersink, B.C. Wilson, G. Zheng, Photodynamic and photothermal therapies: synergy opportunities for nanomedicine, ACS Nano 17 (9) (2023) 7979–8003.
[18] M.R. Younis, C. Wang, R.B. An, S.J. Wang, M.A. Younis, Z.Q. Li, Y. Wang, A. Ihsan, D.J. Ye, X.H. Xia, Low power single laser activated synergistic cancer phototherapy using photosensitizer functionalized dual plasmonic photothermal nanoagents, ACS Nano 13 (2) (2019) 2544–2557.
[19] Z.H. Cai, Y.Q. Fu, Z.L. Qiu, Y. Wang, W.D. Wang, W.X. Gu, Z. Li, S.Y. Wu, F.L. Gao, Multitarget reaction programmable automatic diagnosis and treatment logic device, ACS Nano 15 (12) (2021) 19150–19164.
[20] H.Q. Luo, S. Gao, Recent advances in fluorescence imaging-guided photothermal therapy and photodynamic therapy for cancer: from near-infrared-I to near-infrared-II, J. Controlled Release 362 (2023) 425–445.
[21] Z. He, L.L. Zhao, Q. Zhang, M.J. Chang, C.X. Li, H.S. Zhang, Y. Lu, Y.S. Chen, An acceptor-donor-acceptor structured small molecule for effective NIR triggered dual phototherapy of cancer, Adv. Funct. Mater. 30 (16) (2020) 1910301.
[22] B.Q. Guo, J.L. Zhao, Z.L. Zhang, X. An, M.X. Huang, S.G. Wang, Intelligent nanoenzyme for T1-weighted MRI guided theranostic applications, Chem. Eng. J. 391 (2020) 123609.
[23] J.R. Wu, G.R. Williams, S.W. Niu, Y.B. Yang, Y. Li, X.J. Zhang, L.M. Zhu, Biomineralized bimetallic oxide nanotheranostics for multimodal imaging-guided combination therapy, Theranostics 10 (2) (2020) 841–855.
[24] M.S. Zhang, L. Wang, H. Liu, Z. Wang, W.J. Feng, H. Jin, S.W. Liu, S.J. Lan, Y. Liu, H. Zhang, Copper ion and ruthenium complex codoped polydopamine nanoparticles for magnetic resonance/photoacoustic tomography imaging-guided photodynamic/photothermal dual-mode therapy, ACS Appl. Bio Mater. 5 (5) (2022) 2365–2376.
[25] Y.Y. Pu, Y.D. Zhu, Z. Qiao, N.N. Xin, S.P. Chen, J. Sun, R.R. Jin, Y. Nie, H.S. Fan, A Gd-doped polydopamine (PDA)-based theranostic nanoplatform as a strong MR/PA dual-modal imaging agent for PTT/PDT synergistic therapy, J. Mater. Chem. B 9 (7) (2021) 1846–1857.

[26] Y.X. Guo, Q. Sun, F.G. Wu, Y.L. Dai, X.Y. Chen, Polyphenol-containing nanoparticles: synthesis, properties, and therapeutic delivery, Adv. Mater. 33 (22) (2021) 2007356.

[27] K. Ariga, M. Shionoya, Nanoarchitectonics for coordination asymmetry and related chemistry, Bull. Chem. Soc. Jpn. 94 (3) (2021) 839–859.

[28] X.W. Chen, M. Peng, X.B. Cai, Y.L. Chen, Z.M. Jia, Y.C. Deng, B.B. Mei, Z. Jiang, D. Q. Xiao, X.D. Wen, N. Wang, H.Y. Liu, D. Ma, Regulating coordination number in atomically dispersed Pt species on defect-rich graphene for n-butane dehydrogenation reaction, Nat. Commun. 12 (1) (2021) 2664.

[29] L.Y. Chen, H.F. Wang, C.X. Li, Q. Xu, Bimetallic metal-organic frameworks and their derivatives, Chem. Sci. 11 (21) (2020) 5369–5403.

[30] Y.N. Gong, L. Jiao, Y.Y. Qian, C.Y. Pan, L.R. Zheng, X.C. Cai, B. Liu, S.H. Yu, H. L. Jiang, Regulating the coordination environment of MOF-templated single-atom nickel electrocatalysts for boosting CO_2 reduction, Angewandte Chemie-International Edition 59 (7) (2020) 2705–2709.

[31] B.L. Xu, S.S. Li, L.R. Zheng, Y.H. Liu, A.L. Han, J. Zhang, Z.J. Huang, H.J. Xie, K. L. Fan, L.Z. Gao, H.Y. Liu, A bioinspired five-coordinated single-atom iron nanozyme for tumor catalytic therapy, Adv. Mater. 34 (15) (2022) 2107088.

[32] J. Yang, Y.W. Yang, Metal-organic frameworks for biomedical applications, Small 16 (10) (2020) 1906846.

[33] S.Y. He, L. Wu, X. Li, H.Y. Sun, T. Xiong, J. Liu, C.X. Huang, H.P. Xu, H.M. Sun, W. D. Chen, R. Gref, J.W. Zhang, Metal-organic frameworks for advanced drug delivery, Acta Pharm. Sin. B 11 (8) (2021) 2362–2395.

[34] S. Nooraei, H. Bahrulolum, Z.S. Hoseini, C. Katalani, A. Hajizade, A.J. Easton, G. Ahmadian, Virus-like particles: preparation, immunogenicity and their roles as nanovaccines and drug nanocarriers, J. Nanobiotechnol. 19 (1) (2021) 59.

[35] S. Grabbe, K. Landfester, D. Schuppan, M. Barz, R. Zentel, Nanoparticles and the immune system: challenges and opportunities, Nanomed 11 (20) (2016) 2621–2624.

[36] A.C. Marques, P.J. Costa, S. Velho, M.H. Amaral, Functionalizing nanoparticles with cancer-targeting antibodies: a comparison of strategies, J. Control. Release 320 (2020) 180–200.

[37] M.M. Khan, N. Filipczak, V.P. Torchilin, Cell penetrating peptides: a versatile vector for co-delivery of drug and genes in cancer, J. Control. Release 330 (2021) 1220–1228.

[38] Z.M. Zhao, A. Ukidve, J. Kim, S. Mitragotri, Targeting strategies for tissue-specific drug delivery, Cell 181 (1) (2020) 151–167.

[39] R.H. Fang, W.W. Gao, L.F. Zhang, Targeting drugs to tumours using cell membrane-coated nanoparticles, Nat. Rev. Clin. Oncol. 20 (1) (2023) 33–48.

[40] F. Oroojalian, M. Beygi, B. Baradaran, A. Mokhtarzadeh, M.A. Shahbazi, Immune cell membrane-coated biomimetic nanoparticles for targeted cancer therapy, Small 17 (12) (2021) 2006484.

[41] Y.P. Zeng, S.F. Li, S.F. Zhang, L. Wang, H. Yuan, F.Q. Hu, Cell membrane coated-nanoparticles for cancer immunotherapy, Acta Pharm. Sin. B 12 (8) (2022) 3233–3254.

[42] Y.H. Wu, R.T. Zhu, M.Y. Zhou, J.J. Liu, K. Dong, S.F. Zhao, J.H. Cao, W.J. Wang, C. G. Sun, S.T. Wu, F. Wang, Y.P. Shi, Y.L. Sun, Homologous cancer cell membrane-camouflaged nanoparticles target drug delivery and enhance the chemotherapy efficacy of hepatocellular carcinoma, Cancer Lett. 558 (2023) 216106.

[43] P.P. Xu, H.H. Wu, D.D. Wang, G.Z. Zhao, F.F. Li, B.S. Qiu, Z. Guo, Q.W. Chen, Ultra-small albumin templated Gd/Ru composite nanodots for in vivo dual modal MR/thermal imaging guided photothermal therapy, Adv. Health. Mat. 7 (19) (2018) 1800322.

[44] Y.M. Wang, W. Liu, X.B. Yin, Multifunctional mixed-metal nanoscale coordination polymers for triple-modality imaging-guided photodynamic therapy, Chem. Sci. 8 (5) (2017) 3891–3897.

[45] K.T. Xin, M. Li, D. Lu, X. Meng, J. Deng, D.L. Kong, D. Ding, Z. Wang, Y.J. Zhao, Bioinspired coordination micelles integrating high stability, triggered cargo release, and magnetic resonance imaging, ACS Appl. Mater. Interfaces 9 (1) (2017) 80–91.

[46] Y.P. Shi, M.Y. Zhou, Y. Zhang, Y.F. Wang, J.L. Cheng, MRI-guided dual-responsive anti-tumor nanostructures for synergistic chemo-photothermal therapy and chemodynamic therapy, Acta Biomater. 158 (2023) 571–582.

[47] D. Gao, Y.P. Shi, J.H. Ni, S.J. Chen, Y. Wang, B. Zhao, M.L. Song, X.Q. Guo, X. C. Ren, X.C. Zhang, Z.M. Tian, Z. Yang, NIR/MRI-Guided oxygen-independent carrier-free anti-tumor nano-theranostics, Small 18 (36) (2022) 2106000.

[48] Y.P. Shi, Y. Pan, J. Zhong, J. Yang, J.H. Zheng, J.L. Cheng, R. Song, C.Q. Yi, Facile synthesis of gadolinium (III) chelates functionalized carbon quantum dots for fluorescence and magnetic resonance dual-modal bioimaging, Carbon 93 (2015) 742–750.

[49] M. Hosseini, Z. Ahmadi, A. Kefayat, F. Molaabasi, A. Ebrahimpour, Y.N.K. Far, M. Khoobi, Multifunctional gold helix phototheranostic biohybrid that enables targeted image-guided photothermal therapy in breast cancer, ACS Appl. Mater. Interfaces 14 (33) (2022) 37447–37465.

[50] X.D. Wang, J.Y. Lu, Y.L. Mao, Q.F. Zhao, C.S. Chen, J.A. Han, M.Q. Han, H.J. Yuan, S.L. Wang, A mutually beneficial macrophages-mediated delivery system realizing photo/immune therapy, J. Control. Release 347 (2022) 14–26.